



Article

A Curvature-Based Three-Dimensional Defect Detection System for Rotational Symmetry Tire

Yifei You ^{1,2} , Wenhua Jiao ^{2,*} , Jinglong Chen ³, Zhaoyi Wang ^{1,2}, Xiaofei Liu ⁴, Zhenwen Liu ⁴, Yuantao Chen ⁴ and Xiaofei Zhang ⁴

¹ School of Information and Control Engineering, China University of Mining and Technology, Xuzhou 221116, China; yifeiyou@cumt.edu.cn (Y.Y.); zhaoyiwang@cumt.edu.cn (Z.W.)

² Artificial Intelligence Research Institute, China University of Mining and Technology, Xuzhou 221116, China

³ Shandong Moses Network Technology Co., Ltd., Yantai 265147, China; chenjl@sinomoses.com

⁴ Shandong Linglong Electromechanical Co., Ltd., Zhaoyuan 265406, China; xiaofei_liu@linglong.cn (X.L.); zhenwen_liu@linglong.cn (Z.L.); yuantao_chen@linglong.cn (Y.C.); xiaofei_zhang@linglong.cn (X.Z.)

* Correspondence: wjiao@cumt.edu.cn

Abstract: The efficient detection of tire sidewall defects is crucial for ensuring safety and quality control in manufacturing. Traditional inspection is slow and inconsistent, while automated methods fail to address the complexity and coexistence of multiple tire sidewall defects. To alleviate those shortcomings, this study develops a curvature-based three-dimensional (3D) defect detection system that leverages the inherent rotational symmetry of tire sidewalls, allowing for more accuracy and efficiency in detecting intricate tire sidewall defects. Firstly, a defect detection system is developed that collects the three-dimensional data of tires, enabling precise quality assessments and facilitating accurate defect identification. Secondly, a dataset encompassing various types of intricate tire sidewall defects is constructed. This study leverages normal vectors and surface variation features to conduct an in-depth analysis of the complex three-dimensional shapes of tire sidewalls, while incorporating optimized curvature calculations that significantly enhance detection accuracy and algorithm efficiency. Moreover, the approach enables the simultaneous detection of intricate defect types, such as scratches, transportation damage, and cuts, thereby improving the comprehensiveness and accuracy of the detection process. The experimental results demonstrate that the system achieves a detection accuracy of 95.3%, providing crucial technical support for tire quality control.

Keywords: tire defect detection; curvature; surface variation; 3D point cloud



Citation: You, Y.; Jiao, W.; Chen, J.; Wang, Z.; Liu, X.; Liu, Z.; Chen, Y.; Zhang, X. A Curvature-Based Three-Dimensional Defect Detection System for Rotational Symmetry Tire. *Symmetry* **2024**, *16*, 1581. <https://doi.org/10.3390/sym16121581>

Academic Editor: Hsien-Chung Wu

Received: 4 November 2024

Revised: 15 November 2024

Accepted: 19 November 2024

Published: 26 November 2024



Copyright: © 2024 by the authors. Licensee MDPI, Basel, Switzerland. This article is an open access article distributed under the terms and conditions of the Creative Commons Attribution (CC BY) license (<https://creativecommons.org/licenses/by/4.0/>).

1. Introduction

Tires are indispensable components of vehicles, such as automobiles and airplanes. Their safety and reliability are directly linked to driving security, as well as the safety of passengers and their property. The sidewalls of tires are particularly critical, as defects like scratches, transportation damage, and cuts can adversely affect not only the tire's appearance but also its performance. In extreme cases, these defects may lead to catastrophic failures, including tire blowouts. Thus, detecting sidewall defects is essential, serving as a cornerstone of quality control and a key measure to ensure driving safety while mitigating potential risks [1]. With advancements in intelligent manufacturing and automated detection technologies, tire defect detection has become widely integrated into industrial production processes [2–6], greatly enhancing detection efficiency and accuracy. However, the increasing complexity and variety of tire defects present significant challenges. Efficiently identifying potential defects in a timely manner remains a pressing issue in current research.

Traditional visual inspection approaches [7] involve human inspectors visually examining the tire surface for visible defects, such as cuts or scratches. Inspectors typically

use tools like magnifying glasses or handheld cameras. However, this method is time-consuming, prone to human error, and cannot detect small or hidden defects, especially those on areas that are harder to reach or less visible. The inconsistency in inspection quality can lead to missed defects, which is a significant drawback in large-scale production. Two-dimensional (2D) image processing techniques [2,8–11] capture high-resolution images of the tire surface, which are then analyzed by algorithms to detect visible defects based on patterns, edges, and contrasts. While this method is faster and more consistent than manual inspection, it is limited by its inability to capture depth. The lack of depth information makes it difficult to detect defects that affect the tire's three-dimensional geometry [12], such as small dents or surface cracks that follow the curvature of the tire. X-ray imaging [13–16] allows for the detection of both internal and external defects by passing X-rays through the tire. The resulting image highlights structures inside the tire, such as cracks or air pockets. While this technique can uncover hidden defects, it is expensive, requires specialized equipment, and is complex to operate. Moreover, X-ray imaging is less effective in detecting surface defects like scratches or minor deformations [17], as its resolution is often insufficient for such small, fine details. Moreover, many current detection approaches focus on identifying a single type of defect [18,19], such as scratches or cracks, lacking the capability to comprehensively detect multiple defect types. Tire sidewalls often exhibit various defects simultaneously, including dents, bumps, and cuts as illustrated in Figure 1. The coexistence of these defects complicates detection efforts, as existing technologies struggle to differentiate among multiple defects characterized by complex morphological variations. This limitation significantly affects the comprehensiveness and accuracy of defect detection.

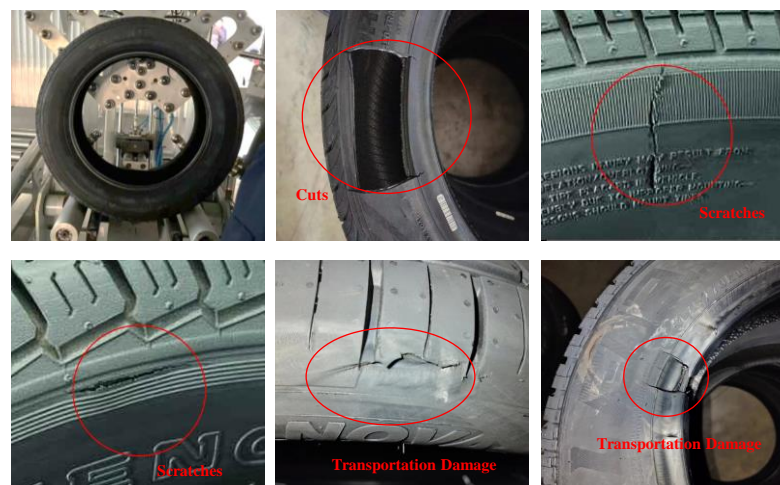


Figure 1. The symmetrical properties of tires and sidewall defects.

To address these limitations, researchers explore three-dimensional scanning technologies to acquire detailed surface data of tires [20,21]. This approach provides a new perspective for defect detection, accurately reflecting the geometric characteristics of tire sidewalls. However, 3D scanning introduces challenges related to complex data processing and substantial computational demands. Efficiently analyzing and processing these data is a significant hurdle in current research. It is worth noting that the geometric structure of tires exhibits high symmetry. This symmetry implies that the tire sidewalls show similar features and performance at different positions. Therefore, utilizing this symmetry in defect detection effectively reduces the complexity of the detection process and enhances the reliability of the detection algorithms. For example, by analyzing the defect characteristics on one side, one can infer the condition of the other side, providing important support for a comprehensive assessment of tire quality. However, despite the theoretical advantage of symmetry, effectively leveraging this characteristic in practical applications remains

a challenge. In tire dynamic balancing, for example, a defect in one area can affect the balance of the entire tire, leading to deformation in the surrounding tread and ultimately compromising safety.

In the tools for describing surface variations, curvature and simple gradient approximations are the primary methods [22]. The gradient is mainly used to describe the rate of change of a surface and is suitable for relatively smooth surfaces. However, it is not sensitive to complex surfaces or local deformations (such as irregular shapes or surface curvature). Therefore, relying solely on gradient methods may not effectively detect small, complex deformations. In contrast, curvature, as a geometric measure, quantifies the local bending of a surface, making it more suitable for capturing these subtle deformations. Curvature analysis has been widely used for defect detection in various industries. For example, in manufacturing, curvature variations are used to detect material deformations and cracks, where even small shape changes can indicate structural issues [23–28]. In the biomedical field, curvature analysis is used to track abnormal tissue changes, such as tumor growth, by detecting minute variations in the shape of biological surfaces [29–31]. These applications demonstrate the potential of curvature analysis in identifying small defects and highlight its usefulness in contexts that require high precision. On the other hand, surface variation refers to changes in texture and relief on a surface, such as roughness, bumps, and dents, which may not be fully captured by curvature analysis alone. Surface variation provides additional insights into the tire's surface conditions, particularly in identifying defects like minor dents and rough areas that are crucial for comprehensive defect detection. For example, in quality control applications, surface variation analysis is used to assess material roughness and surface integrity, revealing defects that curvature measurements might overlook. The combination of curvature and surface variation offers a more holistic approach to defect detection, providing a powerful tool for detecting both geometric features and minor morphological changes on tire sidewalls. However, applying curvature analysis to tire side defect detection presents challenges. For example, the precise modeling and parameterization of tire sidewalls are required, which can be computationally intensive. Previous studies have developed various methods to address this challenge, such as fitting parametric models to the tire's surface and using advanced algorithms for curvature calculation [32,33]. Additionally, the curvature distribution on tire sidewalls is often highly non-uniform, meaning that defect detection algorithms must be adaptable to handle these variations across different regions of the tire surface, which adds complexity to the process.

To overcome these challenges, this study incorporates surface variation features alongside curvature, enhancing detection accuracy and robustness. By considering the geometric symmetry of the tire sidewalls, the detection algorithms can more accurately handle defects in different areas, thereby improving the overall accuracy and consistency of the detection. Furthermore, it emphasizes the importance of simultaneously detecting multiple defect types to facilitate comprehensive tire quality assessments in practical production settings.

The main contributions of this research include the following:

- Development of tire defect detection system: This research led to the creation of a specialized system for detecting tire defects, facilitating accurate assessments of tire quality.
- Construction of a comprehensive dataset: A robust dataset is established, encompassing various types of tire side defects. This dataset serves as a solid foundation for training and validating future detection algorithms.
- Utilization of geometric features: The study leverages geometric features, including normal vectors and surface variation characteristics, to conduct an in-depth analysis of the complex three-dimensional shapes of tire sidewalls. An optimized approach for curvature calculation at feature points is introduced, resulting in improved detection accuracy and algorithm efficiency.
- Simultaneous detection of multiple defect types: The approach enables the simultaneous detection of various defect types—such as scratches, transportation damage,

and cuts—thereby significantly enhancing the comprehensiveness and accuracy of defect detection.

In summary, this research successfully overcomes existing limitations in tire side defect detection, enhancing both accuracy and efficiency through innovative techniques. It provides crucial technical support for tire manufacturing and traffic safety. With ongoing advancements in technology, tire side defect detection is expected to play an increasingly vital role in ensuring driving safety and improving tire quality.

2. Data Acquisition

This section describes the tire defect detection system and dataset production used in this study. We describe in detail the composition of the system, how it works, and the process of making the dataset so as to ensure that high quality tire data are obtained. These data are the basis for subsequent analysis and defect detection.

2.1. Tire Defect Detection System

The tire defect detection system used in this study is composed of a Gocator line laser scanner [32], a bracket structure, a tensioning shaft, and other components. The Gocator line laser scanner specifications are summarized in Table 1. As shown in Figure 2, the device employs a line laser scanner and a video camera based on 3D point cloud imaging technology as part of a multi-sensor system. Specifically, this multi-sensor system consists of a line laser scanner, an optical system, and a camera, all connected to a control system for data transmission and operational control. The multi-sensor system features two independent sub-components for detecting the outer surface and the inner surface of the tire, both equipped with 360-degree sensors for comprehensive inspection without repositioning the tire. The outer and inner surface multi-sensor systems are secured to a stable sensor mounting mechanism to ensure reliable detection results. The outer surface inspection system is connected to the inner surface system by an adjustable lever, allowing for height adjustment based on different tire sizes and types. Notably, the sensors are symmetrically positioned to enhance detection consistency. The outer surface inspection system consists of two sets of line laser scanners positioned on opposite sides of a 180-degree door-frame-shaped plane. The diameter of the door-frame semi-ring structure is greater than the width of the tire under test, ensuring complete coverage of the outer tire area. This design significantly improves the comprehensiveness and accuracy of the test. Figure 3 shows a complete tire point cloud and its local details collected by the tire data detection system. The point cloud represents a three-dimensional image of the tire surface, capturing its intricate features, including tread patterns on the sidewall and irregularities on the side surface. Each point in the point cloud corresponds to a specific location on the tire. The highlighted local details in the figure illustrate areas of particular interest, such as variations in surface texture. At different scales, the details presented in the point cloud vary; as the scale decreases, more details can be observed.

Table 1. Detailed sensor specifications.

Sensor Model	FOV/mm	MR/mm	X-Direction Resolution/ μm	Z-Direction Repeatability/ μm
Gocator2440	96–194	210	67–130	1.2

To ensure consistent tire data, tires with a radius of 14 to 16 inches are used in this study and the camera position is set at 1700 mm. The computing process is performed on an Advantech industrial personal computer (IPC), a public machine equipped with Intel i7-10700TE series processors (Intel Corporation, Santa Clara, CA, USA) and NVIDIA GeForce RTX 3090 graphics (NVIDIA Corporation, Santa Clara, CA, USA). ensuring efficient data processing and high-quality image analysis.

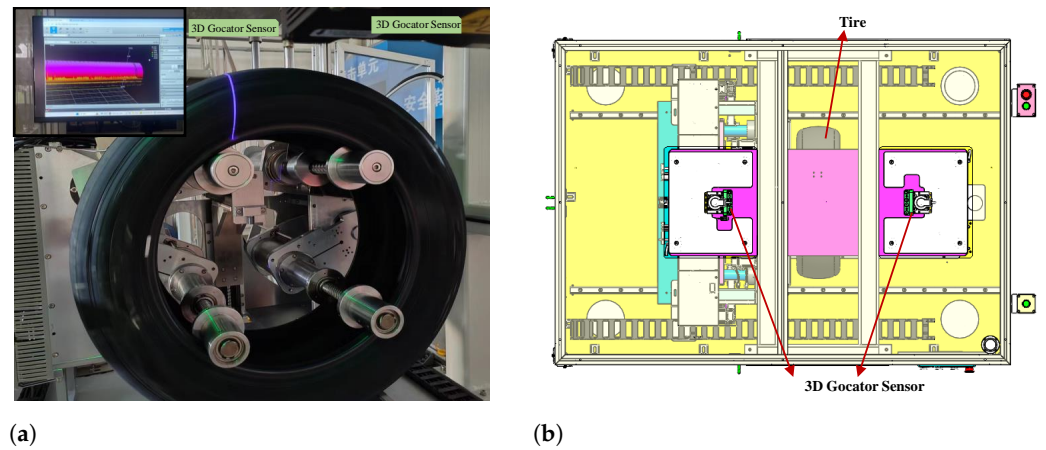


Figure 2. The tire surface defect detection system: (a) a photograph of the device and (b) a top view of the device structure, showing that the sensors are symmetrically positioned on both sides of the tire. Through the operating system, scanning is controlled, and the final results are uploaded to the computer.

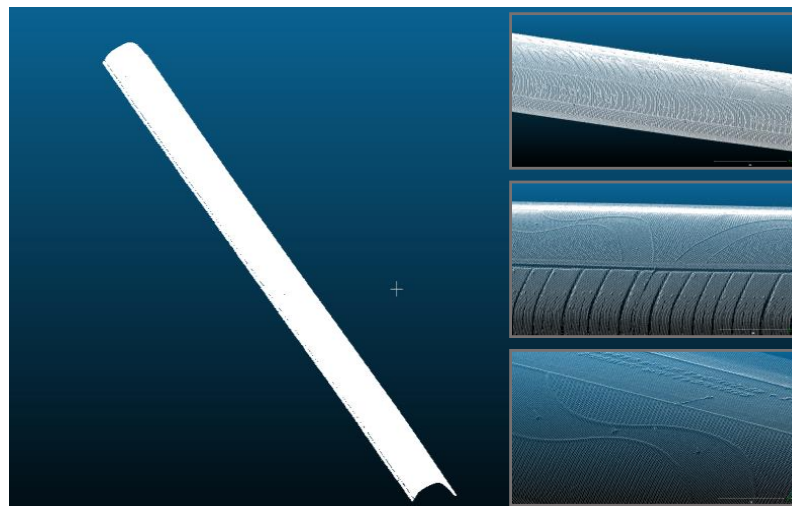


Figure 3. A complete tire point cloud collected by the tire data inspection system, the right side is the point cloud details at different scales.

2.2. Fabrication of Two-Class Dataset for 3D Point Clouds

The datasets used in this paper are sourced from Dezhou Linglong Tire Co., Ltd. (located at Deshang Road East, Economic Development Zone, Wucheng County, Dezhou, Shandong Province, China) covering three types of defects: tire cuts, scratches, and transportation damage. The dataset composition is based on laser 3D scans conducted for each tire. To remove tread fibers and noise during the scanning process, the radius outlier removal [33–35] method is employed.

First, the neighborhood of each center point p_c (a specific point in the point cloud P) is calculated using the following equation:

$$N(p_c) = \{p_j \in P \mid d(p_c, p_j) < r\}, \quad (1)$$

where $N(p_c)$ represents the neighborhood of point p_c , and p_j represents other points in the point cloud p_c such that the Euclidean distance $d(p_c, p_j)$ between point p_c and point p_j is less than the preset radius r .

Next, the number of points in the neighborhood of p_c is calculated as follows:

$$c(p_c) = |N(p_c)|, \quad (2)$$

where $c(p_c)$ denotes the count of points within the neighborhood $N(p_c)$, and k is the minimum number of neighborhood points required for p_c to be retained. If the count $c(p_c)$ is greater than or equal to k , point p_c is retained in the dataset; if it is less than k , point p_c is considered noise and is removed from the dataset.

This process effectively reduces noise in the point cloud data. Figure 4 illustrates the results after tire filtering, showing that noise, such as tread fibers, is successfully filtered out.

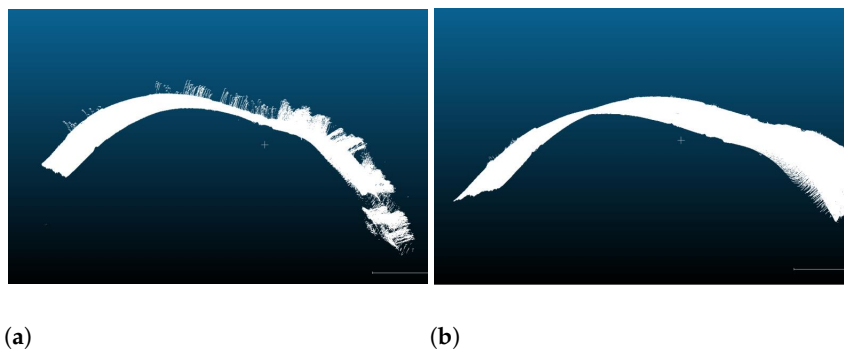


Figure 4. Comparison of filtering effects: (a) image before filtering, showing the presence of impurities and tread fibers; (b) image after filtering, successfully removing impurities and tread fibers.

The dataset production process is shown in Figure 5. The generated point cloud data have a large aspect ratio, which is disadvantageous to the subsequent processing. In addition, the flaw is usually small, but most of the tire area is a normal texture. When extracting features from the original image, the information of normal texture covers the specific information of the flaw, which affects the extraction effect. Therefore, it is necessary to select a suitable window size to ensure that the flaw features can be extracted effectively. For this reason, the sliding window cutting approach is used to intercept the flaws by traversing the whole image. The data are expanded to increase the number of samples. In the process of making the dataset, representative tire bulge defects are selected for detection, and the specific steps are as follows:

1. Standardization of the point cloud file format: The original tire 3D point cloud data obtained by the Gocator line laser scanner are extracted from the information in CSV format and converted to a PLY file in the specified format for subsequent use.
2. Point cloud data preprocessing: The generated point cloud files are further processed, and the radial filter is used to remove the tread fibers and the noise in the scanning process, reducing the interference to the defect classification.
3. Slide cutting: Use a 100 mm × 50 mm × 50 mm sliding window for one-dimensional sliding with a step size of 20 mm to ensure a high overlap rate (60%) and ensure no defects are missed.
4. Flawless image filtering: To maintain a balanced quantity of positive and negative samples, set random filtering conditions. A random integer is generated within a specified range. When this random number falls below a certain threshold, the current image is saved as part of the unblemished dataset.

According to the above process, a total of 92 defect samples are generated, including 23 cut defect clouds, 40 scratch point clouds, 29 transportation losses, and 142 defect-free point clouds.

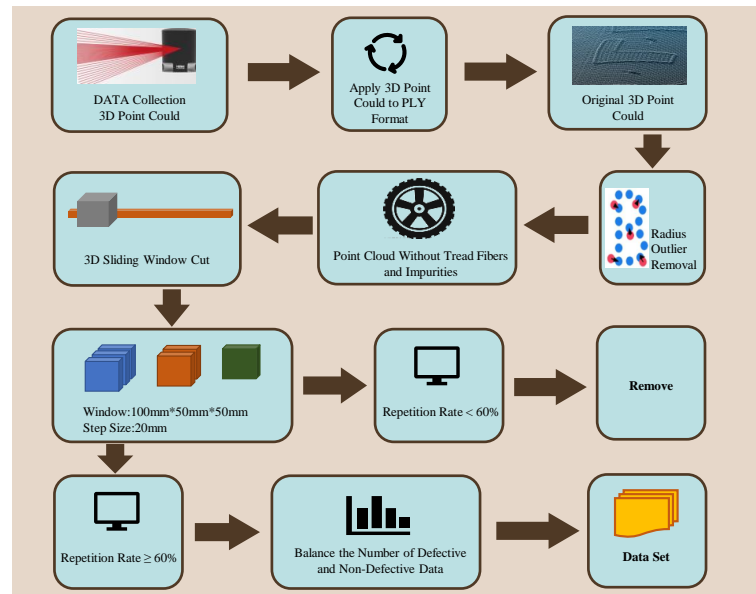


Figure 5. The process of tire 3D point cloud data preprocessing.

3. Materials and Methods

This section describes the methodology of the study in detail, including key calculation steps and feature extraction techniques. We explore how to identify and classify defects on the side of a tire through curvature calculation and other geometric feature extraction. These approaches provide a basis for subsequent data analysis and interpretation of the results.

3.1. Curvature Calculation and Feature Extraction

In 3D point clouds, principal component analysis (PCA) [36–38] can be used to estimate normal vectors from the local neighborhood of points. The process includes the following steps.

Firstly, as illustrated in Figure 6, for a given center point p_c , we select the points in its neighborhood, forming the set (p_1, p_2, \dots, p_n) , where the coordinates of each point are given by (x_j, y_j, z_j) for $j = 1, 2, \dots, n$. We can calculate the mean of these neighborhood points as the centroid of the neighborhood point set:

$$\bar{p} = \frac{1}{n} \sum_{j=1}^n p_j = \left(\frac{1}{n} \sum_{j=1}^n x_j, \frac{1}{n} \sum_{j=1}^n y_j, \frac{1}{n} \sum_{j=1}^n z_j \right), \quad (3)$$

where \bar{p} is the centroid of the neighborhood points, and p_j represents the j -th point in the neighborhood.

Next, we calculate the covariance matrix C using the neighborhood points and the centroid \bar{p} :

$$C = \frac{1}{n} \sum_{j=1}^n (p_j - \bar{p})(p_j - \bar{p})^T. \quad (4)$$

The covariance matrix C is a 3×3 symmetric matrix that represents the dispersion of the local point cloud. It is a core step of PCA and is used to analyze the principal directions of the point set. The expanded form of the covariance matrix C is

$$C = \begin{pmatrix} C_{xx} & C_{xy} & C_{xz} \\ C_{yx} & C_{yy} & C_{yz} \\ C_{zx} & C_{zy} & C_{zz} \end{pmatrix}, \quad (5)$$

where the elements are calculated as follows:

$$C_{xx} = \frac{1}{n} \sum_{j=1}^n (x_j - \bar{x})^2, \quad (6)$$

$$C_{yy} = \frac{1}{n} \sum_{j=1}^n (y_j - \bar{y})^2, \quad (7)$$

$$C_{zz} = \frac{1}{n} \sum_{j=1}^n (z_j - \bar{z})^2, \quad (8)$$

$$C_{xy} = \frac{1}{n} \sum_{j=1}^n (x_j - \bar{x})(y_j - \bar{y}), \quad (9)$$

$$C_{xz} = \frac{1}{n} \sum_{j=1}^n (x_j - \bar{x})(z_j - \bar{z}), \quad (10)$$

$$C_{yz} = \frac{1}{n} \sum_{j=1}^n (y_j - \bar{y})(z_j - \bar{z}), \quad (11)$$

where C_{xy} , C_{xz} , and C_{yz} represent the covariance between the respective coordinate axes.

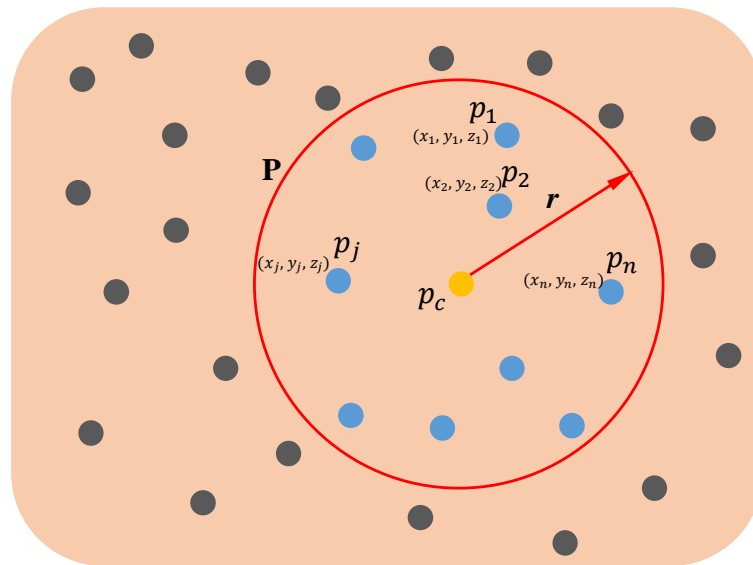


Figure 6. Random center point p_c and all neighborhood points within a radius r along with their coordinates.

Through eigenvalue decomposition of the covariance matrix C , we obtain the eigenvalues $\lambda_1, \lambda_2, \lambda_3$ and the corresponding eigenvectors v_1, v_2, v_3 . These eigenvectors represent the dominant directions of the point set, while the eigenvalues indicate the degree of dispersion along these directions. The eigenvalue problem can be expressed as $Cv = \lambda v$. The larger the eigenvalue, the greater the scatter of the point set in that direction. The eigenvalues are sorted from large to small: $\lambda_1 \geq \lambda_2 \geq \lambda_3$. The eigenvector corresponding to the smallest eigenvalue λ_3 is considered the normal vector n_c of the point p_c .

In practice, the direction of the normal vector may be affected by noise. Therefore, the normal vectors of multiple points in the neighborhood are usually averaged to improve

stability. The specific approach involves performing a weighted average on the normal vectors of the neighboring points:

$$v_s = \frac{1}{n} \sum_{j=1}^n v_j, \quad (12)$$

where v_s is the smoothed normal vector for the point p_c (the current point for which we are estimating the normal vector), and v_j represents the normal vectors of the n neighboring points around p_c . By smoothing the normal vector, the stability of the normal estimation can be improved, reducing the influence of noise on the calculated normal.

3.2. Multi-Scale Analysis

In order to address defects of different sizes, this study is implemented through multi-scale curvature calculation. Given different neighborhood radii r , curvature characteristics at various scales can be calculated separately. For each scale r , the corresponding curvature H [30] is computed, and the robustness of the defect detection is enhanced through multi-scale fusion.

To compute these curvatures on a discrete point cloud, they are typically approximated by fitting a quadric surface to the points in the neighborhood. The quadratic equation can be expressed as

$$z = ax^2 + by^2 + cxy + dx + ey + f, \quad (13)$$

where a, b, c, d, e , and f are coefficients to be determined, x and y are the independent variables, and z represents the value of the surface at coordinates (x, y) . The adjacent points $\{p_1, p_2, \dots, p_n\}$ are used to minimize the error and fit this surface. The curvature H of the surface can be derived from the coefficients a, b, c :

$$H = \frac{(1 + d^2)b + (1 + e^2)a - dec}{(1 + d^2 + e^2)^{3/2}}. \quad (14)$$

The multi-scale curvature calculations can be expressed as

$$H_r = \frac{H(r_1) + H(r_2) + \dots + H(r_n)}{n} \quad (15)$$

where H_r represents the average curvatures at scale r , and $H(r_n)$ denotes the curvatures computed at different neighborhood scales r_n . The parameter r indicates the neighborhood range at various scales.

By employing this multi-scale analysis approach, the system can synthesize local and global geometric information, thereby enhancing the capability to detect complex defects. Furthermore, fusing the curvature features from different scales improves the adaptability and robustness of the detection algorithm to shape changes, enabling the effective handling of various tire defects in practical applications.

3.3. Surface Variation Feature Optimized Curvature Calculation

Surface variation is an important index used to characterize the degree of surface change in the neighborhood of a point [39,40]. By analyzing the normal vectors of the points in the neighborhood, local abrupt change regions on the surface can be effectively identified, reflecting potential defects.

To define the neighborhood, we let P be the set of all points in the point cloud, and for a center point p_c , its neighborhood $N(p_c)$ can be expressed as

$$N(p_c) = \{p_j \in P \mid d(p_c, p_j) < r\}, \quad (16)$$

where r is a predefined radius. For each point p_j in this neighborhood, we can calculate its normal vector v_j .

Firstly, the normal vector in the neighborhood of the point p_c is calculated. The surface variation $SV(p_c)$ can then be computed using the following formula:

$$SV(p_c) = \frac{1}{n} \sum_{j=1}^n \|v_c - v_j\|, \quad (17)$$

where n is the number of points in the neighborhood, v_c is the normal vector of the point p_c , and v_j is the normal vector of other points p_j in the neighborhood. This formula computes the average distance between the normal vector of point p_c and the normal vectors of each point in its neighborhood.

A high value of surface variation indicates a significant change in the normal vector, which may suggest defects or abrupt changes in the surface, such as dents, bulges, or cracks. Conversely, low values indicate that the area is relatively smooth, with minimal variation, typically corresponding to a normal tire surface.

To further enhance the detection capability of surface variation, a weighted calculation of the normal vector can be introduced. Specifically, each neighborhood point p_j may be assigned a weight w_j , adjusted according to its distance from the center point p_c . The weighted surface variation $SV_w(p_c)$ can be expressed as

$$SV_w(p_c) = \frac{1}{n} \sum_{j=1}^n w_j \|v_c - v_j\|, \quad (18)$$

where the weight $w_j = \frac{1}{1+d(p_c, p_j)}$ can be calculated using the formula, and $d(p_c, p_j)$ is the distance between points p_c and p_j . Then, the curvature is

$$Tr = H_r + k \cdot SV_w(p_c) \quad (19)$$

where Tr represents the decision threshold which is a metric that represents the integrated curvature at each point p_c on the surface, with k representing the weighting coefficients that determine the relative influence of the surface variation $SV(p_c)$ and the weighted surface variation $SV_w(p_c)$ on the curvature calculation.

By incorporating both the weighted surface variation and curvature, we enhance the sensitivity to subtle changes in surface geometry. This approach ensures that the curvature measurements accurately reflect the local conditions around p_c , thereby improving the overall defect detection capabilities. A defect threshold D is established such that if Tr exceeds D , the point is classified as a defect; otherwise, it is considered defect free.

3.4. Overall Inspection Framework

To achieve efficient and accurate tire defect detection, this study has constructed an automated detection system that integrates curvature and surface change characteristics. As shown in Figure 7, the system design emphasizes the close connection between each step to form a complete detection process.

First, the system preprocesses the point cloud data of the tire surface, estimating the normal vectors and performing denoising to ensure data quality. Next, it calculates curvature for each point using multi-scale analysis, thereby extracting rich geometric features that enhance the sensitivity and accuracy of defect detection.

Subsequently, the system combines curvature features and surface change indicators to achieve the simultaneous detection of multiple defect types. Utilizing a machine learning model, the system automatically identifies defects such as scratches, transportation damage, and cutting surfaces, significantly improving detection efficiency and accuracy.

Finally, upon completion of the inspection, the system optimizes the results and automatically generates a detailed inspection report that includes defect types, locations, and their impacts, providing a vital reference for subsequent quality control.

In summary, the main steps of the overall detection framework include the following:

1. Point cloud preprocessing, including normal vector estimation and denoising.
2. The calculation of curvature for each point based on multi-scale analysis.
3. The simultaneous detection of multiple defects using curvature characteristics and surface variations.
4. The optimization of test results and the output of a detailed tire defect inspection report.

This approach enables the capture of complex geometric features on the tire's side at different scales, facilitating the accurate identification of multiple defect types. This overall framework aims to enhance detection efficiency and accuracy, meeting the high standards of tire quality required in industrial production.

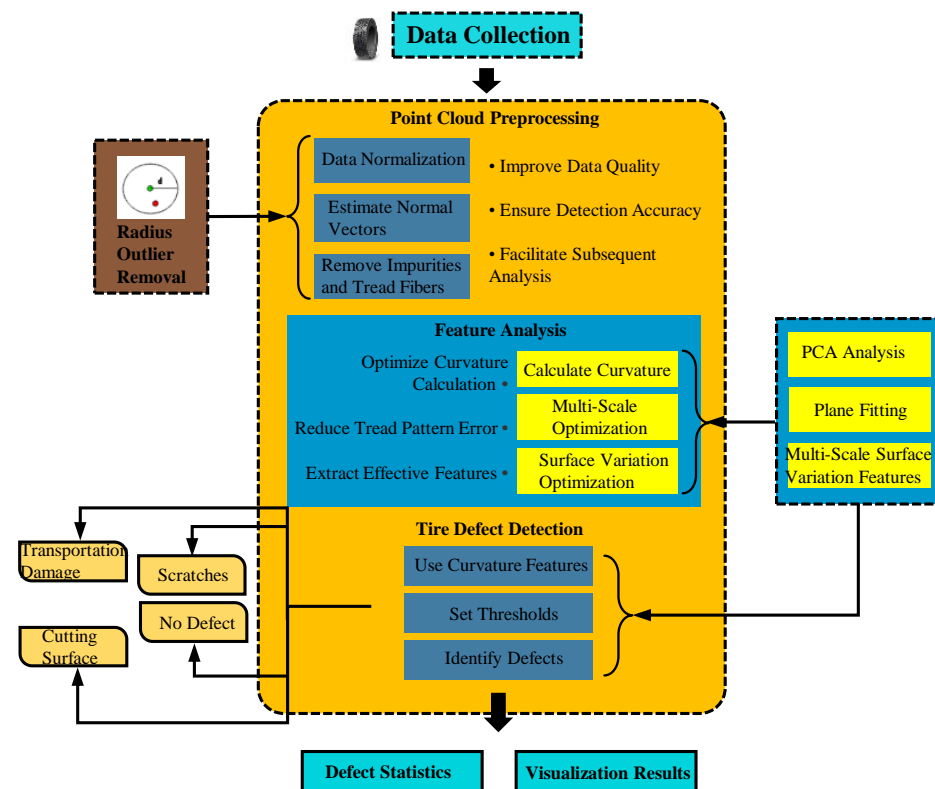


Figure 7. Tire curvature feature analysis and defect detection framework.

4. Results and Discussion

In this section, we discuss the findings of this study, focusing on curvature calculation and defect detection. By examining sidewall defects such as scratches, cuts, and transportation damage, we aim to highlight their potential impact on tire performance and safety.

4.1. Curvature Calculation

4.1.1. Multi-Scale Curvature Variation

In this study, curvature calculation serves as a crucial step in detecting tire defects. By estimating surface normals and calculating curvature from point cloud data, we capture local geometric features of the tire surface, laying the groundwork for subsequent defect identification. To analyze subtle changes in the tire surface more comprehensively, we compute the curvature at various scales. This multi-scale approach allows us to better capture the diversity and complexity of the defects. Curvature is calculated across different neighborhood radii to identify small-scale local defects as well as larger-scale deformations. Experimental results show that as the neighborhood scale increases, the curvature features

exhibit significant variation, particularly in sidewall regions where bulges or depressions are present, leading to more pronounced curvature discontinuities.

As shown in Figure 8, at smaller scales, the curvature features primarily reflect minor defects such as fine scratches, while at larger scales, they effectively identify more prominent scratches. However, when the neighborhood size is too small (less than 0.5 mm), the curvature calculation becomes overly sensitive, highlighting minor surface variations that may not be relevant to defect detection. On the other hand, when the neighborhood size is too large (greater than 8 mm), important defect features can be missed, as the curvature calculation becomes too generalized and smooth, making it difficult to distinguish subtle defects from the overall surface. Figure 9 illustrates that the curvature value distributions calculated at different radii vary significantly. In regions without defects, the curvature values tend to be low, indicating a smoother surface that is closer to a plane. However, as the radius increases, the curvature calculated for each point decreases, which may overlook important geometric features. Larger radii can cause the loss of finer details, such as tread patterns or subtle surface irregularities, which are crucial for effective defect detection.

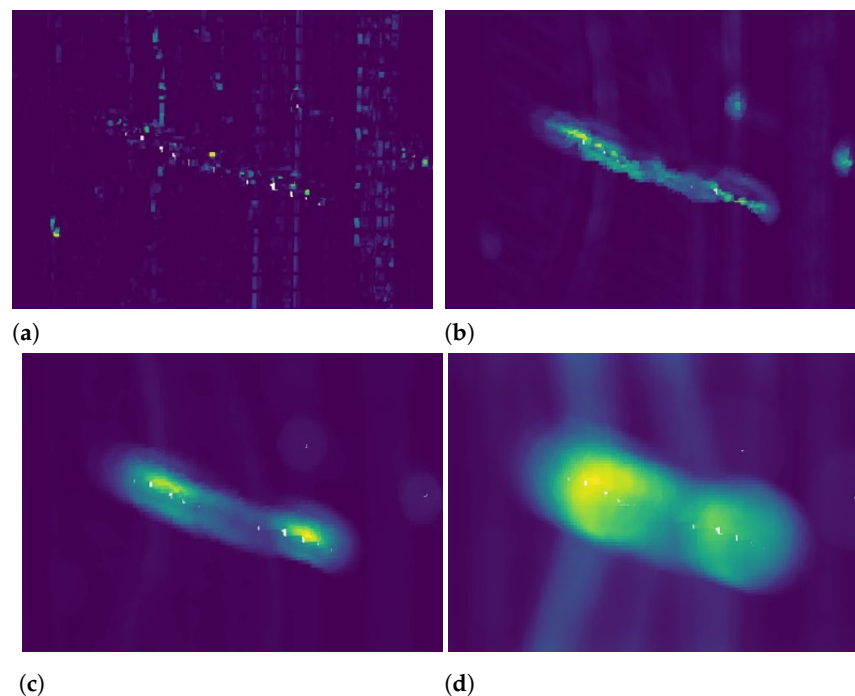


Figure 8. The curvature feature maps of scratch defects at different radii are shown: (a) calculation result for radius $r = 0.5$ mm, (b) calculation result for radius $r = 2$ mm, (c) calculation result for radius $r = 4$ mm, (d) calculation result for radius $r = 8$ mm.

Conversely, when the radius is very small, the curvature calculation can become inaccurate. At smaller radii, while more geometric features are represented, the limited number of neighboring points can lead to instability in the curvature values. This can result in erratic measurements that do not reliably reflect the true surface geometry, making it challenging to distinguish between normal variations and actual defects. To overcome these challenges, multi-scale fusion is employed to combine different neighborhood sizes, typically using radii of 0.5, 2.0, 4.0, and 8.0. This combination allows for a more accurate and balanced representation of defects across various scales. By leveraging information from multiple radii, the method effectively highlights defect features at different levels of detail, while minimizing noise and instability. This approach improves the robustness and accuracy of the defect detection process by ensuring that both fine surface irregularities and larger, more prominent defects are adequately captured.

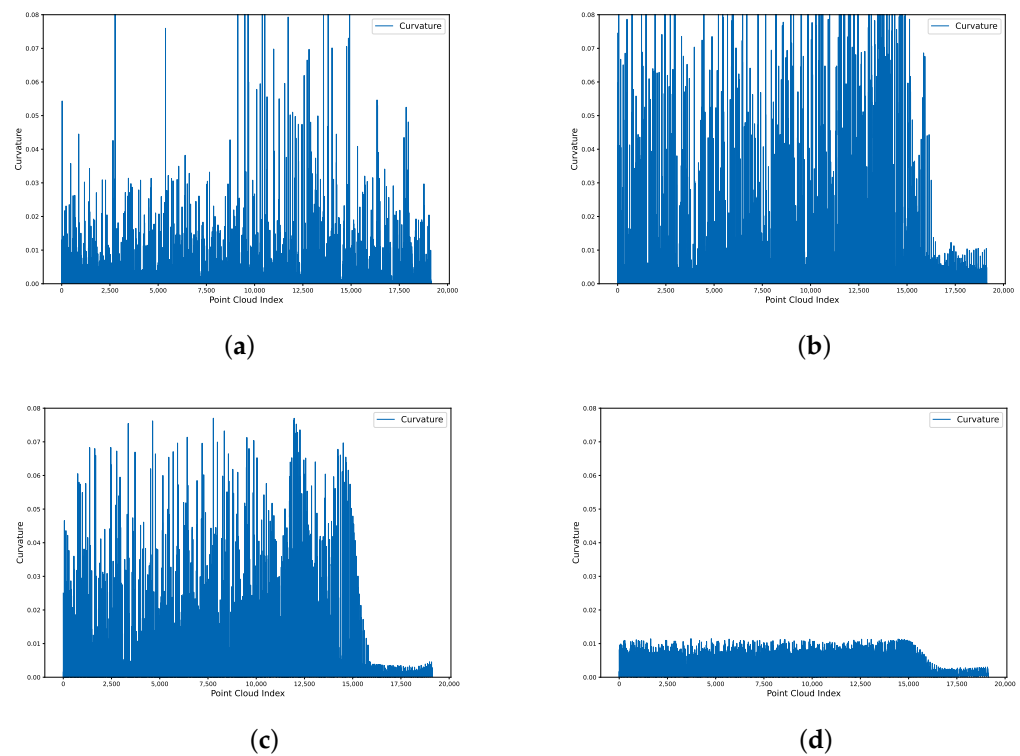


Figure 9. The curvature values of scratch defects at different radii are shown: (a) calculation result for radius $r = 0.5$ mm, (b) calculation result for radius $r = 2$ mm, (c) Calculation result for radius $r = 4$ mm, (d) calculation result for radius $r = 8$ mm.

Therefore, by combining curvature features at different radii, we effectively capture complex geometric characteristics through multi-scale fusion. This approach allows us to integrate both fine details and broader surface trends, enhancing our ability to detect and characterize defects.

As shown in Figure 10, Figure 10a presents the original point cloud of the untreated defects, which may not fully convey the intricate boundary details. In contrast, Figure 10b displays the point cloud after multi-scale fusion, clearly illustrating how this method captures the boundary features of the defects more effectively. The multi-scale fusion process not only improves the visibility of defect boundaries but also helps distinguish between genuine defects and normal surface variations. By leveraging information from various scales, we enhance the robustness and accuracy of the defect detection process, ensuring that critical features are not overlooked. This comprehensive representation of the surface geometry significantly contributes to the overall effectiveness of our defect detection methodology.

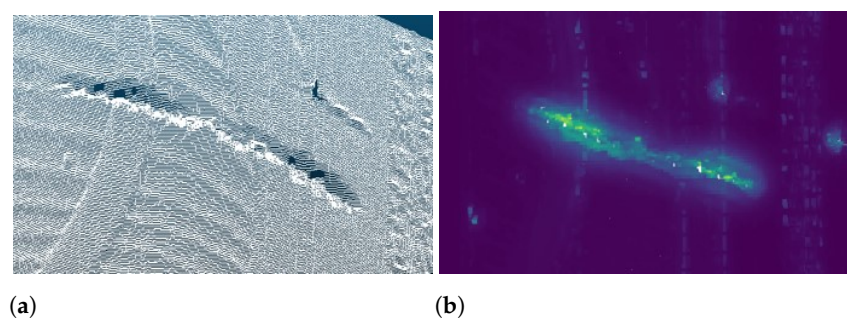


Figure 10. Defect curvature features after multi-scale fusion. (a) Original point cloud of untreated defects, with insufficient boundary detail. (b) Point cloud after multi-scale fusion, clearly displaying defect boundaries.

4.1.2. Surface Variation Feature Optimization Effects

Although the curvature features after multi-scale fusion clearly capture the boundary characteristics of defects, relying solely on curvature features is insufficient to distinguish defects from tread patterns and sidewall markings. Therefore, the introduction of surface variation features provides important supplementary information for defect identification. By calculating the changes in normal vectors within a neighborhood, surface variation features capture subtle geometric changes, leading to more accurate identification of tire surface defects.

In practical applications, we conduct a comparative analysis of different types of defects. Experimental results show that surface variation features excel in distinguishing small defects (such as scratches and minor dents), particularly in areas where boundaries are ambiguous or resemble normal textures. By combining curvature and surface variation features, we achieve higher detection accuracy in complex backgrounds.

As shown in Figure 11, the optimized surface variation feature map illustrates significant changes in different regions of the defect point cloud. The horizontal axis represents the feature values, while the vertical axis indicates the number of points corresponding to these feature values.

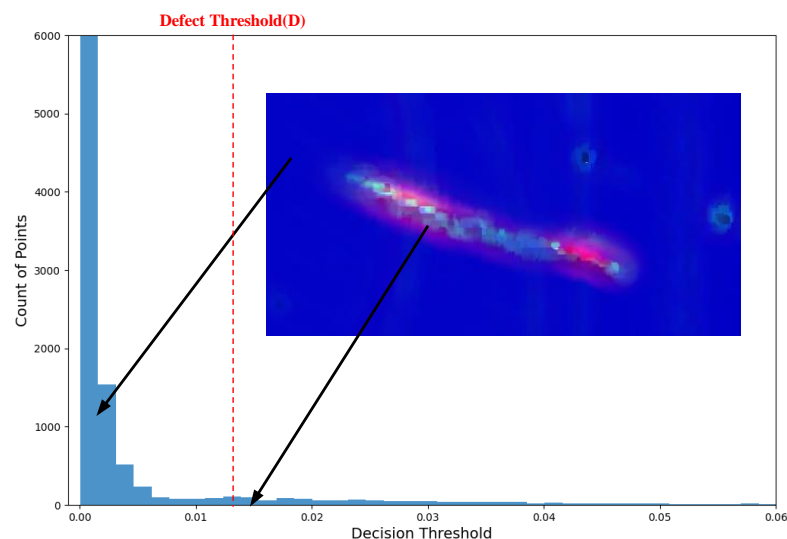


Figure 11. Optimized surface variation feature map. The surface variation feature values of the normal tread pattern range from 0 to 0.013, while the feature values of the defective areas are above 0.013.

In Figure 11, the feature differences between the defect areas and the surrounding normal regions are significant. Higher feature values indicate pronounced geometric changes in these areas, while the feature values of the defect-free tread portions are relatively concentrated and stable. By quantifying these changes, we clearly identify the shape and location of the defects.

By optimizing the surface variation features, our detection system significantly improves in accuracy and robustness, particularly when dealing with challenging tire surfaces. This approach enhances the sensitivity of defect detection and effectively reduces the false positive rate, providing a reliable basis for subsequent quality control and safety assessments.

Moreover, the introduction of surface variation features enables the detection system to dynamically adjust its detection strategy when facing different types of defects. For example, when detecting scratches, the system prioritizes areas with significant normal vector changes, while for larger defects, it combines curvature features for comprehensive judgment. This flexible detection strategy makes the system more efficient and reliable in practical applications.

In summary, the effective combination of surface variation features and curvature features enhances the performance of defect detection and provides more precise support for tire quality assessment and safety monitoring.

4.2. Detection Results of Multiple Defects

In this study, we successfully implemented the automated detection of various defects on the sidewall of tires, including scratches, cuts, and transport damage. By utilizing the aforementioned curvature calculation and surface variation analysis approaches, combined with the fusion of multi-scale features, we determined that the defect threshold D for segmenting defects from the sidewall was 0.013. By setting this threshold for defect detection, our detection system demonstrated outstanding performance.

First, by processing the collected 3D point cloud data, we were able to accurately identify various flaws on the tire surface. As shown in Table 2, the system achieved an accuracy of 96.6% for detecting transport damage, while the accuracies for scratches and cuts were 82.5% and 87%, respectively. The overall defect detection accuracy was 86%, and the overall detection accuracy reached 95.3%. These results validate the effectiveness of employing multi-scale curvature and surface variation features.

Table 2. Summary of defect detection results.

Types	Number	Correct Detection	Accuracy
Transport damage	29	28	96.6%
Scratches	40	33	82.5%
cuts	23	20	87%
Defect-free	142	142	100%
Total	234	223	95.3%

Additionally, we provided visual images of different types of defects as illustrated in Figure 12. The figure highlights several types of defects identified by the system, including scratches, cuts, and transport damage. Each defect type is clearly marked, showcasing the effectiveness of our multi-scale curvature fusion and feature optimization techniques. In the figure, the scratched areas are marked in vibrant colors, allowing for clear identification of their length and depth, which reflect their potential impact on tire performance. The transport damage region displays surface deformations and material damage, emphasizing the risks that can arise during transportation. The images of the cuts reveal irregularities and their significance for structural integrity. These annotations not only detail the specific defect types but also illustrate the progression from raw point cloud data to refined defect detection. This transformation demonstrates how our methodology enhances the clarity of defects, making them easier to identify. Notably, after applying these methods, the sidewall defects become significantly distinguishable, especially in areas with subtle geometric changes. The images in the figure provide a comprehensive overview of the defects, revealing complex details such as the length of scratches, the extent of transport damage, and the irregularities found on the cuts.

To further validate the reliability of the detection results, we compared the system's output with manually annotated data. By calculating the overlap rate between the detected defects and actual flaws, we found that the detection system maintained high accuracy even in complex environments. This comparison confirms the scientific rigor and practical applicability of our detection approach, ensuring its accuracy under various conditions.

Moreover, the system demonstrated excellent real-time performance, with the entire detection process averaging only 3 s, making it well suited for rapid application on industrial production lines. This provides tire manufacturers with an efficient and reliable quality control tool.

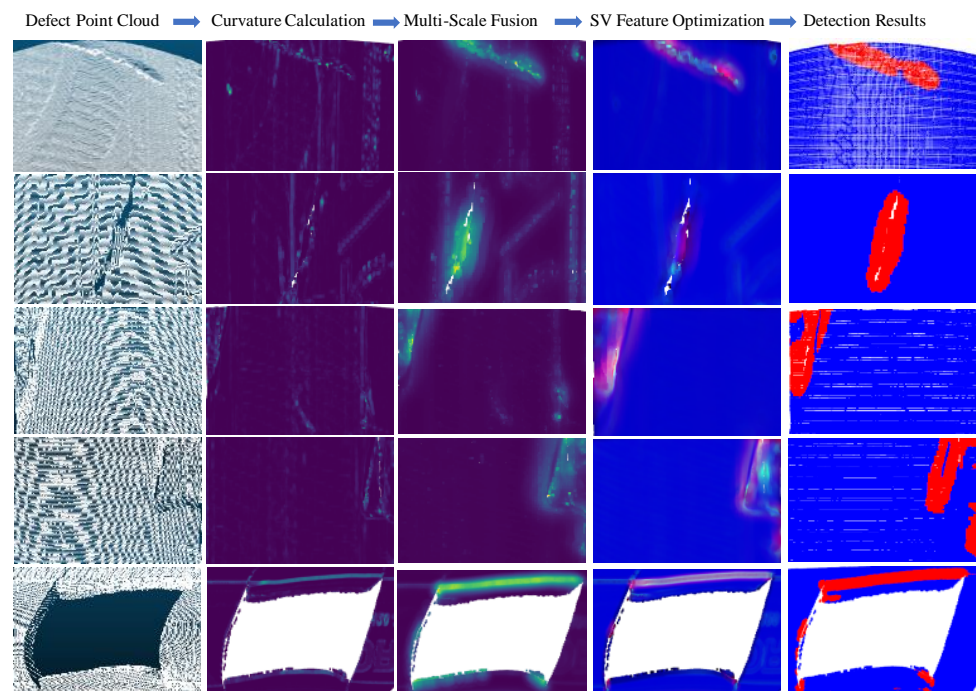


Figure 12. Visualization of different types of defects, including scratches, cuts, and transport damage.

In summary, the defect detection approach proposed in this study effectively identifies various tire defects in real-world applications, providing strong support for enhancing tire safety and performance.

4.3. False Detection Analysis

In practical applications, although our defect detection system demonstrates high accuracy, false detection is still inevitable. To better understand the reasons behind such false detection and improve detection performance, we conduct a detailed analysis of the cases of false detection. As shown in Table 2, the accuracy for detecting scratches is the lowest among all defect types, prompting us to focus our analysis on the false detections related to scratches.

First, during the detection of complex tire side patterns or markings, a significant issue is that the system tends to misidentify the normal geometric features in these areas as defects. This misjudgment mainly occurs in regions with high curvature variations, where the visual characteristics closely resemble those of defects. Specifically, as shown in Figure 13, we can observe the following points:

1. Visual similarity (Figure 13a): The tire side patterns are visually very close to potential defects, making it difficult for the system to distinguish them based solely on appearance.
2. Overlapping curvature features (Figure 13b): The curvature features of defects highly overlap with those of the patterns, further complicating the system's judgment.
3. Similarity in surface variation features (Figure 13c): In finer surface variation features, the characteristics of defects remain similar to those of the patterns, further blurring the system's ability to recognize defects.

The root of this misjudgment lies in the significant overlap of features between defects and the background, specifically, the tire side patterns or markings. This overlap creates ambiguity in the system's judgment, making it difficult for the system to accurately distinguish normal features from defect features, ultimately resulting in false detections.

Furthermore, the likelihood of false detections increases when the detection system processes surface reflections or lightly damaged defects. For instance, surface reflections

can introduce noise or interference in the 3D point cloud data, impacting the system's ability to accurately identify defects. This issue is particularly prevalent in smooth areas of the tire side, where reflected light can lead to local misjudgments, especially under varying lighting conditions.

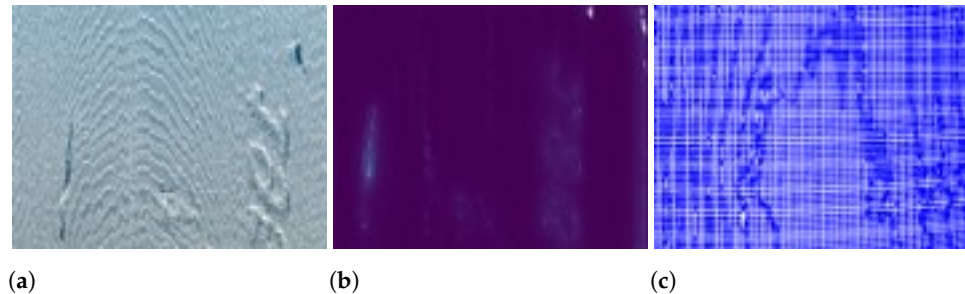


Figure 13. Analysis of false detection in tire side patterns: (a) visual similarity, (b) curvature overlap, and (c) surface variation features.

Additionally, the risk of false detections is higher for small defects, such as scratches and minor dents, due to their relatively small geometric features and lack of clear contrast with normal textures. In complex textured backgrounds, identifying small defects becomes even more challenging, as the system may mistakenly classify noise or texture details as defects.

For transportation damage and cuts defects, while their characteristics are more pronounced, overlapping features at the edges with surrounding normal areas can occur. This phenomenon may lead the system to misinterpret the boundaries of defects, thereby affecting overall detection accuracy.

To address these false detections, we will continue to optimize the algorithm to enhance the system's resistance to interference when dealing with tires that exhibit complex textures and optical properties. Future research will focus on developing customized detection strategies tailored to the feature differences among various types of defects, aiming to improve the accuracy and robustness of identifying minor defects. Through these improvements, we expect to significantly reduce the false detection rate and enhance the reliability and practicality of the defect detection system.

5. Conclusions

This study presents an advanced approach to tire defect detection. By designing a tire defect detection device that utilizes the symmetrical properties of tires, the system effectively obtains point cloud data to identify various defects, including scratches, cuts, and transport damage. Leveraging geometric features such as curvature and surface variation, along with a multi-scale feature fusion method, the system comprehensively captures surface defect characteristics, achieving high accuracy in defect detection while significantly reducing the false detection rate. Recognizing the importance of tire symmetry, the approach also contributes to tire dynamic balancing, ensuring that defects do not compromise the overall stability of the tire. Through a comprehensive analysis of the detection results, we identify key factors leading to false detections, including surface reflections, the complexity of tire patterns, and variations in lighting conditions.

In the future, we aim to further enhance the detection algorithms by addressing the challenges posed by surface reflections, complex tire patterns, and lighting variations. Additionally, we plan to focus on improving the system's robustness to handle diverse environments, particularly real-world scenarios in which vehicles are in operation. This could significantly reduce the number of traffic accidents caused by unnoticed tire defects, such as cuts, cracks, and deformations, which compromise tire safety. Moreover, by developing customized detection strategies tailored to different defect types, we will contribute to automating tire quality control and further enhancing tire safety across the automotive industry.

Author Contributions: Conceptualization, Y.Y. and W.J.; approaches, Y.Y.; software, Y.Y., J.C. and W.J.; validation, Y.Y., W.J. and Z.W.; formal analysis, Y.Y.; investigation, Y.Y. and Z.W.; resources, J.C., X.L., Z.L., Y.C. and X.Z.; data curation, Y.Y. and Z.W.; writing—original draft preparation, Y.Y.; writing—review and editing, Y.Y. and W.J.; visualization, Y.Y.; supervision, W.J.; project administration, W.J. and J.C.; funding acquisition, W.J. All authors have read and agreed to the published version of the manuscript.

Funding: This work is supported by 2022 Yantai science and technology innovation plan under grant No. 2022ZDCX008.

Data Availability Statement: Restrictions apply to the datasets. The datasets presented in this article are not readily available because the data are part of an ongoing study. Requests to access the datasets should be directed to the corresponding author’s email.

Conflicts of Interest: Author Jinglong Chen is employed by the Shandong Moses Network Technology Co., Ltd. Authors Xiaofei Liu, Zhenwen Liu, Yuantao Chen and Xiaofei Zhang are employed by the Shandong Linglong Electromechanical Co., Ltd. The remaining authors declare that the research was conducted in the absence of any commercial or financial relationships that could be construed as a potential conflict of interest.

References

1. Weysenhoff, A.; Opala, M.; Koziak, S.; Melnik, R. Characteristics and Investigation of Selected Manufacturing Defects of Passenger Car Tires. *Transp. Res. Procedia* **2019**, *40*, 119–126. [[CrossRef](#)]
2. Aguilar, J.J.C.; Carrillo, J.A.C.; Fernández, A.J.G.; Pozo, S.P. Optimization of an Optical Test Bench for Tire Properties Measurement and Tread Defects Characterization. *Sensors* **2017**, *17*, 707. [[CrossRef](#)] [[PubMed](#)]
3. Bialer, O.; Tirer, T. Performance Analysis of Automotive SAR With Radar Based Motion Estimation. *IEEE Trans. Veh. Technol.* **2023**, *72*, 11332–11345. [[CrossRef](#)]
4. Du, C.; Li, F.; Shi, Y.; Yang, C.; Gui, W. Integral Event-Triggered Attack-Resilient Control of Aircraft-on-Ground Synergistic Turning System With Uncertain Tire Cornering Stiffness. *IEEE CAA J. Autom. Sin.* **2023**, *10*, 1276–1287. [[CrossRef](#)]
5. Ji, Y.; Zeng, J.; Ren, L. Research on the Prediction of Tire Radial Load Based on 1D CNN and BiGRU. *Int. J. Comput. Intell. Syst.* **2023**, *16*, 185. [[CrossRef](#)]
6. Han, J.-Y.; Kwon, J.-H.; Lee, S.; Lee, K.C.; Kim, H.J. Experimental Evaluation of Tire Tread Wear Detection Using Machine Learning in Real-Road Driving Conditions. *IEEE Access* **2023**, *11*, 32996–33004. [[CrossRef](#)]
7. Ren, Z.; Fang, F.; Yan, N.; Wu, Y. State of the Art in Defect Detection Based on Machine Vision. *Int. J. Precis. Eng. Manuf.-Green Tech.* **2022**, *9*, 661–691. [[CrossRef](#)]
8. Li, G.; Zheng, Z.; Shao, Y.; Shen, J.; Zhang, Y. Automated Tire Visual Inspection Based on Low Rank Matrix Recovery. *Multimed. Tools Appl.* **2023**, *82*, 24227–24246. [[CrossRef](#)]
9. Chang, C.-Y.; Wang, W.-C. Integration of CNN and Faster R-CNN for Tire Bubble Defects Detection. In *Advances on Broadband and Wireless Computing, Communication and Applications, Proceedings of the 13th International Conference on Broadband and Wireless Computing, Communication and Applications, BWCCA 2018, Taichung, Taiwan, 27–29 October 2018*; Barolli, L., Leu, F.-Y., Enokido, T., Chen, H.-C., Eds.; Springer: Berlin/Heidelberg, Germany, 2018; Volume 25, pp. 285–294.
10. Ho, C.-H.; Huang, Z.; Kim, N.; Bae, Y.-S.; Vasconcelos, N. Tire Defect Detection with Limited Annotation. In *Proceedings of the Intelligent Robotics and Industrial Applications Using Computer Vision 2021, San Francisco, CA, USA, 15–19 January 2023*; Society for Imaging Science and Technology: Springfield, VA, USA, 2023; pp. 1–6.
11. Cui, X.; Liu, Y.; Zhang, Y.; Wang, C. Tire Defects Classification with Multi-Contrast Convolutional Neural Networks. *Int. J. Pattern Recognit. Artif. Intell.* **2018**, *32*, 1850011. [[CrossRef](#)]
12. Kuric, I.; Klarák, J.; Sága, M.; Císar, M.; Hajdučík, A.; Wiecek, D. Analysis of the Possibilities of Tire-Defect Inspection Based on Unsupervised Learning and Deep Learning. *Sensors* **2021**, *21*, 7073. [[CrossRef](#)]
13. Zhao, G.; Qin, S. High-Precision Detection of Defects of Tire Texture Through X-ray Imaging Based on Local Inverse Difference Moment Features. *Sensors* **2018**, *18*, 2524. [[CrossRef](#)] [[PubMed](#)]
14. Wang, Y.; Zhang, Y.; Zheng, L.; Yin, L.; Chen, J.; Lu, J. Unsupervised Learning with Generative Adversarial Network for Automatic Tire Defect Detection from X-ray Images. *Sensors* **2021**, *21*, 6773. [[CrossRef](#)] [[PubMed](#)]
15. Wang, R.; Guo, Q.; Lu, S.; Zhang, C. Tire Defect Detection Using Fully Convolutional Network. *IEEE Access* **2019**, *7*, 43502–43510. [[CrossRef](#)]
16. Gao, S.; Dai, Y.; Xu, Y.; Chen, J.; Liu, Y. Generative Adversarial Network-Assisted Image Classification for Imbalanced Tire X-ray Defect Detection. *Trans. Inst. Meas. Control* **2023**, *45*, 1492–1504. [[CrossRef](#)]
17. Chen, J.; Li, Y.; Zhao, J. X-ray of Tire Defects Detection via Modified Faster R-CNN. In *Proceedings of the 2019 2nd International Conference on Safety Produce Informatization (IICSPI), Chongqing, China, 28–30 November 2019*; pp. 257–260.
18. Lin, Y.-H.; Ruan, S.-J. A Tiny Defect Detection System for Tire Mold Surfaces Based on Consecutive Frames. *IEEE Trans. Instrum. Meas.* **2023**, *72*, 1–8. [[CrossRef](#)]

19. Yang, S.; Jiao, D.; Wang, T.; He, Y. Tire Speckle Interference Bubble Defect Detection Based on Improved Faster RCNN-FPN. *Sensors* **2022**, *22*, 3907. [[CrossRef](#)]
20. Armeni, I.; Sener, O.; Zamir, A.R.; Jiang, H.; Brilakis, I.; Fischer, M.; Savarese, S. 3D Semantic Parsing of Large-Scale Indoor Spaces. In Proceedings of the 2016 IEEE Conference on Computer Vision and Pattern Recognition (CVPR), Las Vegas, NV, USA, 27–30 June 2016; pp. 1534–1543.
21. Wu, Z.; Song, S.; Khosla, A.; Yu, F.; Zhang, L.; Tang, X.; Xiao, J. 3D ShapeNets: A Deep Representation for Volumetric Shapes. In Proceedings of the 2015 IEEE Conference on Computer Vision and Pattern Recognition (CVPR), Boston, MA, USA, 7–12 June 2015; pp. 1912–1920.
22. Guo, Y.; Bennamoun, M.; Sohel, F.; Lu, M.; Wan, J. 3D Object Recognition in Cluttered Scenes with Local Surface Features: A Survey. *IEEE Trans. Pattern Anal. Mach. Intell.* **2014**, *36*, 2270–2287. [[CrossRef](#)] [[PubMed](#)]
23. Sang, M.; Wang, W.; Pan, Y. RGB-ICP Method to Calculate Ground Three-Dimensional Deformation Based on Point Cloud from Airborne LiDAR. *Remote Sens.* **2022**, *14*, 4851. [[CrossRef](#)]
24. Moosavi-Dezfooli, S.-M.; Fawzi, A.; Uesato, J.; Frossard, P. Robustness via Curvature Regularization, and Vice Versa. In Proceedings of the 2019 IEEE/CVF Conference on Computer Vision and Pattern Recognition (CVPR), Long Beach, CA, USA, 15–20 June 2019; pp. 9070–9078.
25. Barua, S.; Mahmoud, K.; El-Salakawy, E. Slender GFRP-RC Circular Columns under Concentric, Eccentric, and Flexural Loads: Experimental Investigation. *J. Bridge Eng.* **2021**, *26*, 4021033. [[CrossRef](#)]
26. Li, H.; Cao, J.; Zhu, J.; Liu, Y.; Zhu, Q.; Wu, G. Curvature Graph Neural Network. *Inf. Sci.* **2022**, *592*, 50–66. [[CrossRef](#)]
27. Chen, Z.; Lu, Y.; Manica, R.; Liu, Q. Curvature Effects on Liquid–Solid Contact Electrification. *Nano Energy* **2021**, *89*, 106456. [[CrossRef](#)]
28. Gundogdu, E.; Constantin, V.; Parashar, S.; Seifoddini, A.; Dang, M.; Salzmann, M.; Fua, P. GarNet++: Improving Fast and Accurate Static 3D Cloth Draping by Curvature Loss. *IEEE Trans. Pattern Anal. Mach. Intell.* **2022**, *44*, 181–195. [[CrossRef](#)] [[PubMed](#)]
29. Rodriguez, M.; Swiekatowski, K.; Tung, R.; Nguyen, P. Applying Artificial Intelligence to Facial Curvature Analysis for Gender-Affirming Surgery. *Plast. Reconstr. Surg. Glob. Open* **2023**, *11*, 109. [[CrossRef](#)]
30. Yu, S.-M.; Oh, J.M.; Lee, J.; Lee-Kwon, W.; Jung, W.; Amblard, F.; Granick, S.; Cho, Y.-K. Substrate Curvature Affects the Shape, Orientation, and Polarization of Renal Epithelial Cells. *Acta Biomater.* **2018**, *77*, 311–321. [[CrossRef](#)]
31. Yue, X.; Robert, S.; Ungerleider, L.G. Curvature Processing in Human Visual Cortical Areas. *NeuroImage* **2020**, *222*, 117295. [[CrossRef](#)]
32. Wang, J.; Zhang, Q.; Yang, B.; Zhang, B. Vision-Based Automated Recognition and 3D Localization Framework for Tower Cranes Using Far-Field Cameras. *Sensors* **2023**, *23*, 4851. [[CrossRef](#)] [[PubMed](#)]
33. Goh, P.Y.; Tan, S.C.; Cheah, W.P.; Lim, C.P. Adaptive Rough Radial Basis Function Neural Network with Prototype Outlier Removal. *Inf. Sci.* **2019**, *505*, 127–143. [[CrossRef](#)]
34. Prio, M.H.; Patel, S.; Koley, G. Implementation of Dynamic Radius Outlier Removal (DROR) Algorithm on LiDAR Point Cloud Data with Arbitrary White Noise Addition. In Proceedings of the 2022 IEEE 95th Vehicular Technology Conference: (VTC2022-Spring), Helsinki, Finland, 19–22 June 2022; pp. 1–7.
35. Duan, Y.; Yang, C.; Li, H. Low-Complexity Adaptive Radius Outlier Removal Filter Based on PCA for Lidar Point Cloud Denoising. *Appl. Opt.* **2021**, *60*, E1–E7. [[CrossRef](#)]
36. Li, W.; Peng, M.; Wang, Q. Improved PCA Method for Sensor Fault Detection and Isolation in a Nuclear Power Plant. *Nucl. Eng. Technol.* **2019**, *51*, 146–154. [[CrossRef](#)]
37. Jafarzadegan, M.; Safi-Esfahani, F.; Beheshti, Z. Combining Hierarchical Clustering Approaches Using the PCA Method. *Expert Syst. Appl.* **2019**, *137*, 1–10. [[CrossRef](#)]
38. Mrówczyńska, M.; Sztubecki, J.; Greinert, A. Compression of Results of Geodetic Displacement Measurements Using the PCA Method and Neural Networks. *Measurement* **2020**, *158*, 107693. [[CrossRef](#)]
39. Abanov, A.G.; Monteiro, G.M. Free-Surface Variational Principle for an Incompressible Fluid with Odd Viscosity. *Phys. Rev. Lett.* **2019**, *122*, 154501. [[CrossRef](#)] [[PubMed](#)]
40. Etim, U.J.; Bai, P.; Wang, Y.; Subhan, F.; Liu, Y.; Yan, Z. Mechanistic Insights into Structural and Surface Variations in Y-Type Zeolites upon Interaction with Binders. *Appl. Catal. A Gen.* **2019**, *571*, 137–149. [[CrossRef](#)]

Disclaimer/Publisher’s Note: The statements, opinions and data contained in all publications are solely those of the individual author(s) and contributor(s) and not of MDPI and/or the editor(s). MDPI and/or the editor(s) disclaim responsibility for any injury to people or property resulting from any ideas, methods, instructions or products referred to in the content.